Electronic Supplementary Material (ESI) for Journal of Materials Chemistry A.

Supporting Information

Harvesting solar energy by Ni-MOF-based evaporator for efficient solar thermal storage and steam generation

*You Xu [a], , Zhengyun Wang [a], Xianbao Wang [b], Zhenzhen Guo [b], Muhammad Sultan Irshad [b], Naila Arshad [b,c] , Jiang Gong [a, *], Hongfang Liu [a, *], Guangfang Li [a, *]*

[a] Key Laboratory of Material Chemistry for Energy Conversion and Storage, Ministry of Education, Hubei Key Laboratory of Material Chemistry and Service Failure, Hubei Engineering Research Center for Biomaterials and Medical Protective Materials, School of Chemistry and Chemical Engineering, Huazhong University of Science and Technology, Wuhan 430074, P. R. China

[b] Ministry of Education Key Laboratory for the Green Preparation and Application of Functional Materials, Hubei Key Laboratory of Polymer Materials (Hubei University), Collaborative Innovation Center for Advanced Organic Chemical Materials Co-constructed By the Province and Ministry, School of Materials Science and Engineering, Hubei University, Wuhan 430062, PR China

[c] Institute of Quantum Optics and Quantum Information, School of Science, Xi'an Jiaotong University (XJTU), Xi'an 710049, China

Analysis of heat transfer processes

Thermal analysis for the solar vapor desalination process is conducted, including the effective energy for evaporation (Q_{Evap}), conductive heat loss to bulk water (Q_1), convective (Q_2) and radiative (Q_3) heat loss to the surroundings.

The energy dynamic equilibrium can be expressed as:

$$A \alpha q_{Solar} = Q_{Evap} + Q_1 + Q_2 + Q_3 \quad \text{(S1)}$$

where A denotes the surface area of absorber facing the sun, α solar absorbance, and q_{Solar} input solar flux

The conductive heat loss to bulk water (Q_1) can be calculated through the temperature gradient in the underlying water:

$$Q_1 = Cm(Tl1 - Tl2) \quad \text{(S2)}$$

where C represents the specific heat capacity of water (4.2 kJ K^{-1} kg^{-1}), and m denotes the weight of water (g). The temperature gradient in the underlying water below the samples is measured by two embedded thermocouples under one sun (i.e., $Tl1$=17.3 °C and $Tl2$= 16.8 °C). In this work, m= 95 g, ΔT= 0.5 K. Consequently, the Q_1 is ca. 2.53%.

The convective heat loss (Q_2) to the adjacent environment can be calculated by Newton' law of cooling:

$$Q_2 = A\, h\, (T_a - T_\infty) \quad \text{(S3)}$$

where h is convection heat transfer coefficient (assumed to be 5 W m^{-2} K^{-1}), T_a (31.5 °C) is the top surface temperature of absorber, and T_∞ is the average side temperature of evaporator at a steady state condition under one sun. Since the light-absorbing material is surrounded by water layer and hot vapor, the adjacent temperature can be approximated as the vapor temperature (i.e., $T_\infty = T_{vapor}$= 26.5°C). Consequently, the Q_2 is calculated to be 25.0 W m^{-2}, corresponding 2.57%.

The radiative heat loss (Q_3) to the ambient environment can be calculated by Stefan-Boltzmann law:

$$Q_3 = A\, \varepsilon\, \sigma(T_a^4 - T_{vapor}^4) \quad \text{(S4)}$$

where ε denotes the ε is the emissivity, and emissivity in this equation is supposed has a maximum emissivity of 1. σ is the Stefan-Boltzmann constant (5.669×10^{-8} W m^{-2}

K^{-4}). Consequently, the Q_3 is calculated to be 31.59 W m^{-2}, corresponding 3.25%. Therefore, the heat loss of NMC-PCM-3 in the water evaporation is 8.35%.

Analysis of water evaporation enthalpy

To measure the water evaporation enthalpy, the water loss in the dark within 1 h was recorded, in which the evaporators receive the same energy from the environment to convert liquid water to vapor. Considering the known theoretical evaporation enthalpy of liquid water (ca. 2434 J g^{-1}), the enthalpy of blank-PCM-2 and NMC-PCM-2 is calculated by the formula:

$$U_{\mathrm{I}} = E_{\mathrm{equ}} m_{\mathrm{g}} = E_0 m_0 \quad \text{(S5)}$$

where U_{I} in is the total energy absorbed from the environment per hour; E_0 and m_0 refer to the water evaporation enthalpy (J g^{-1}) and the mass loss (g) of water in 1 h without NMC-PCM-2 in the dark, respectively; m_{g} means the water loss (g) of NMC-PCM-2 while E_{equ} is the equivalent evaporation enthalpy (J g^{-1}).

Figures and tables

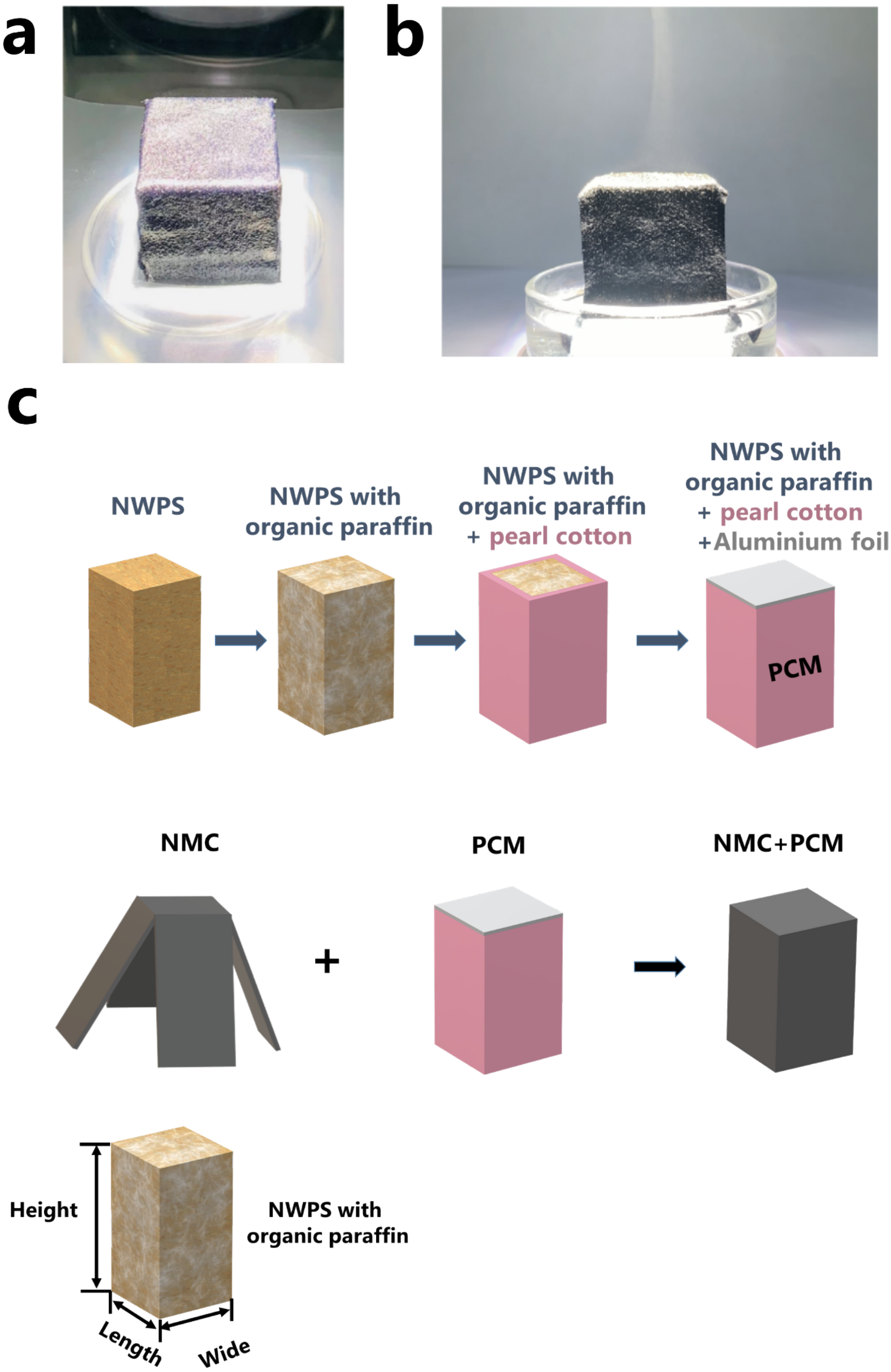

Figure S1. (a-b) Digital photographs of NMC-PCM evaporator for efficient solar steam generation. (c) Schematic structure of the 3D evaporator.

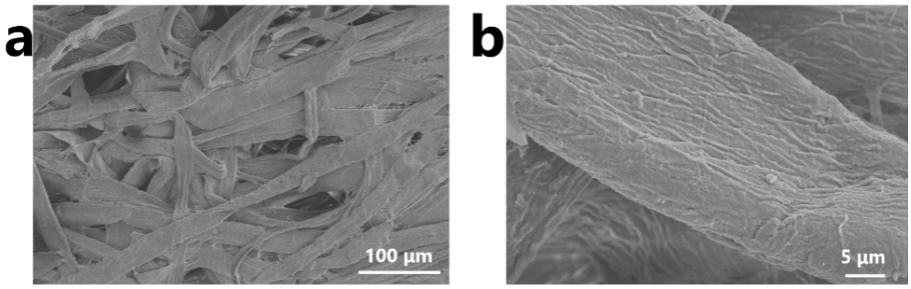

Figure S2. SEM images of the air-laid paper.

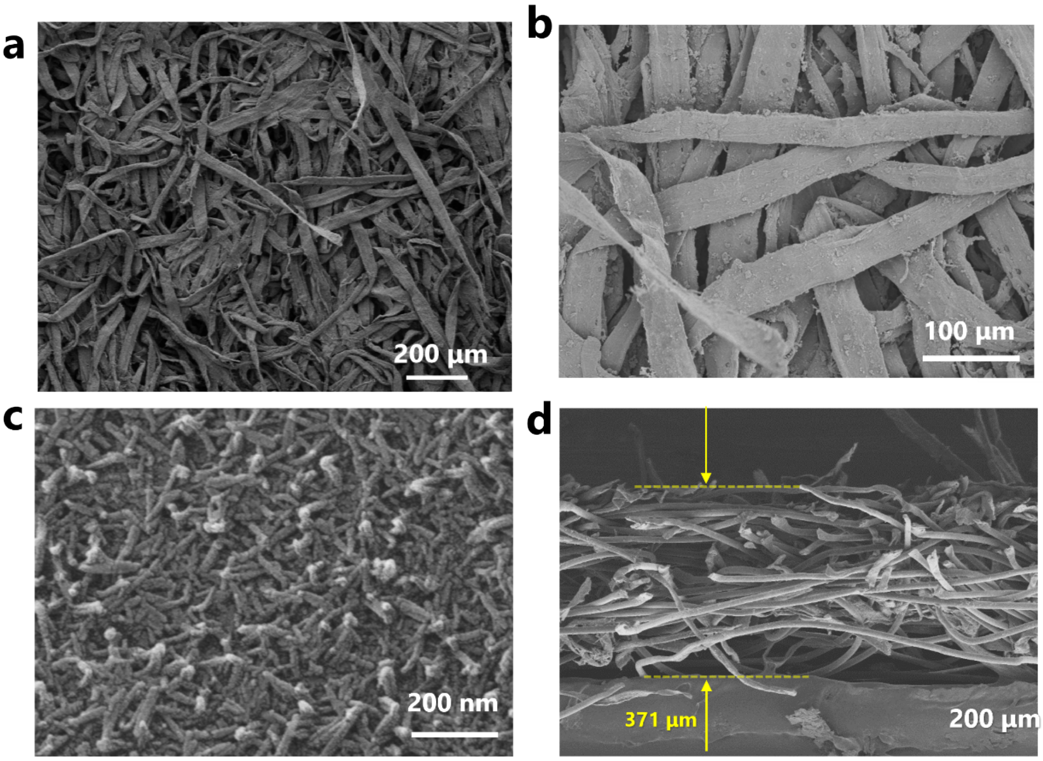

Figure S3. (a-c) SEM image of the NMC and (d) cross sectional SEM image of the NMC.

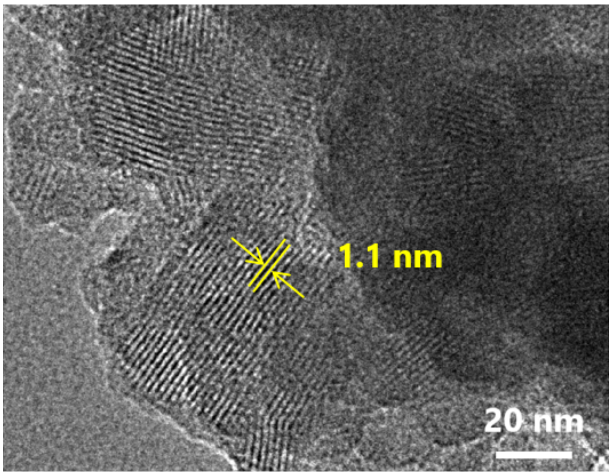

Figure S4. HRTEM image of the NMC.

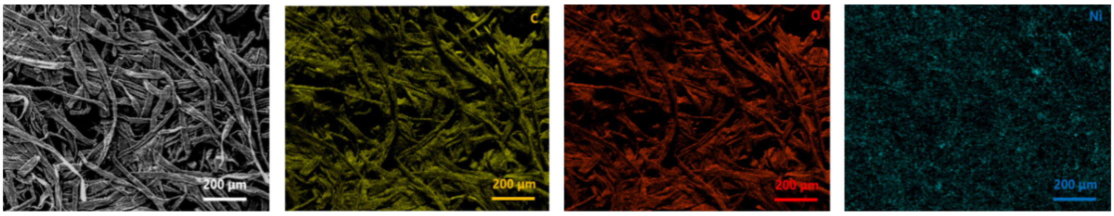

Figure S5. EDX elemental mapping results of the NMC.

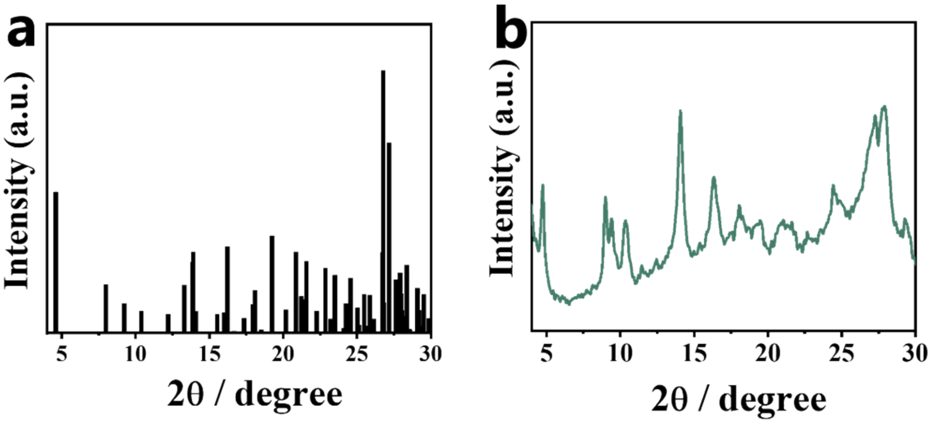

Figure S6. XRD patterns of (a) the standard peaks for Ni-CAT-1 MOF crystals and (b) the Ni-CAT MOF.

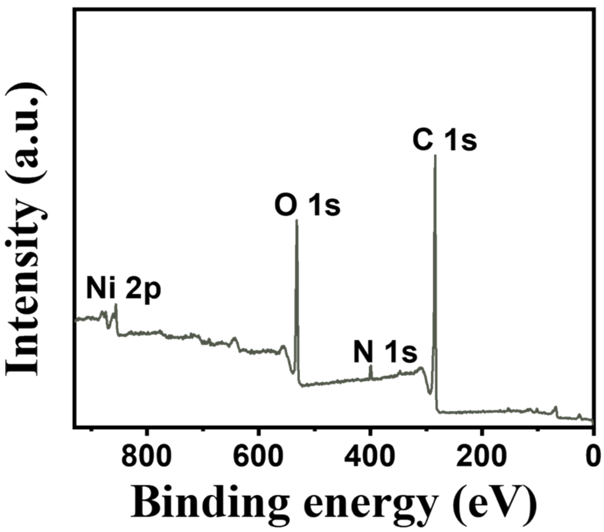

Figure S7. XPS survey spectrum of the NMC.

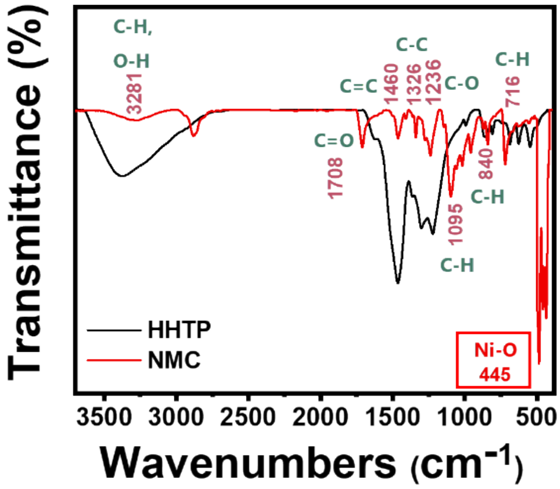

Figure S8. FTIR spectrum of the HHTP and NMC.

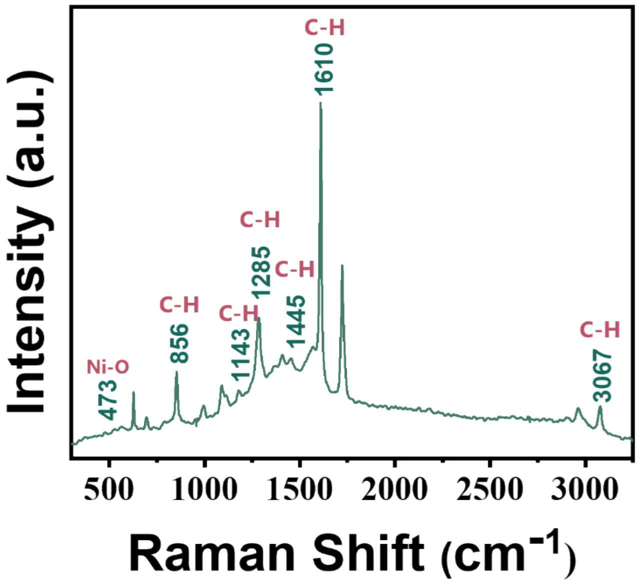

Figure S9. Raman spectrum of the NMC.

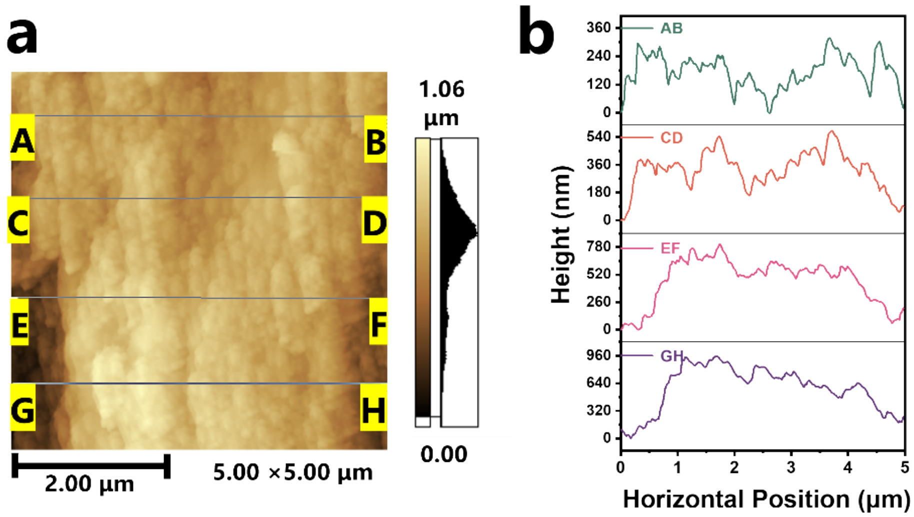

Figure S10. AFM scans of a 5 µm × 5 µm area of the NMC with a color bar displaying the film heights and (B) height distribution of the corresponding line segments.

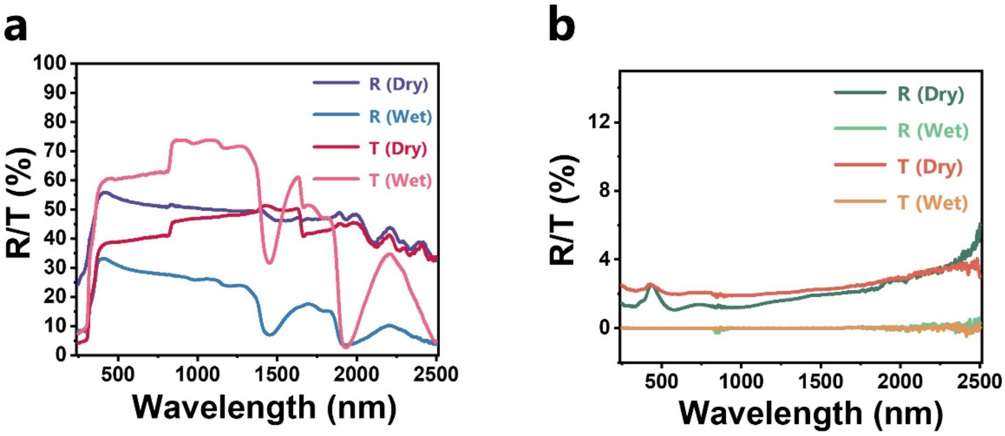

Figure S11. Reflectance and transmittance spectra of the wet/dry state (a) air-laid paper and (b) NMC in the wavelength range of 250-2500 nm.

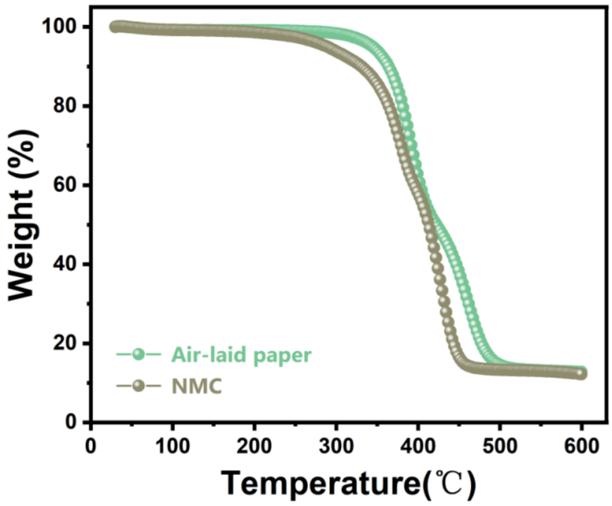

Figure S12. Thermogravimetric analysis (TGA) of the air-laid paper and NMC from 30 to 600 ℃ in N_2 atmosphere.

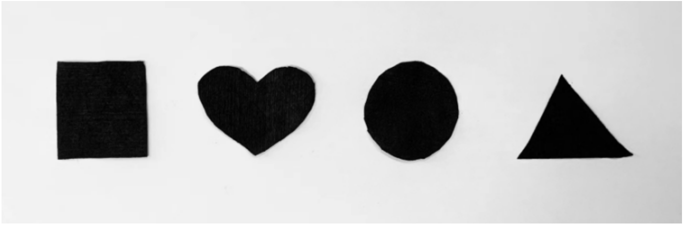

Figure S13. Scheme of various patterning models.

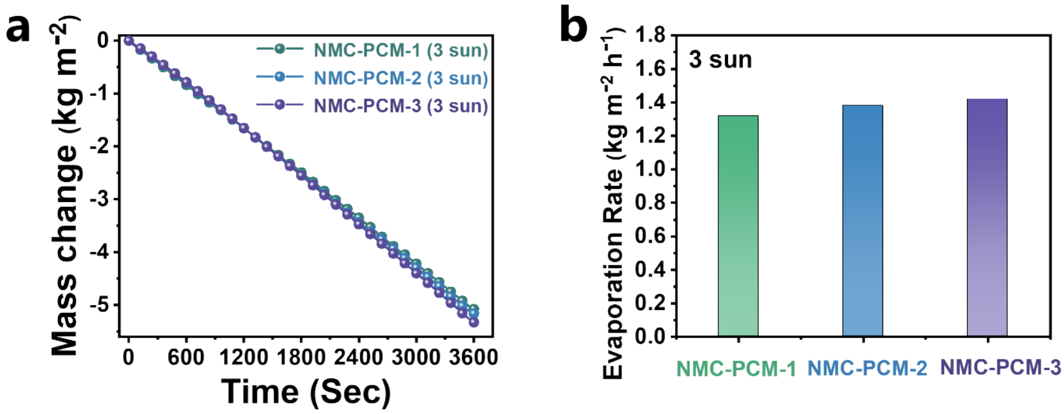

Figure S14. (a) Time-dependent mass change of NMC-PCM-1/2/3 under three sun illumination and (b) evaporation rate of after turning off the light source.

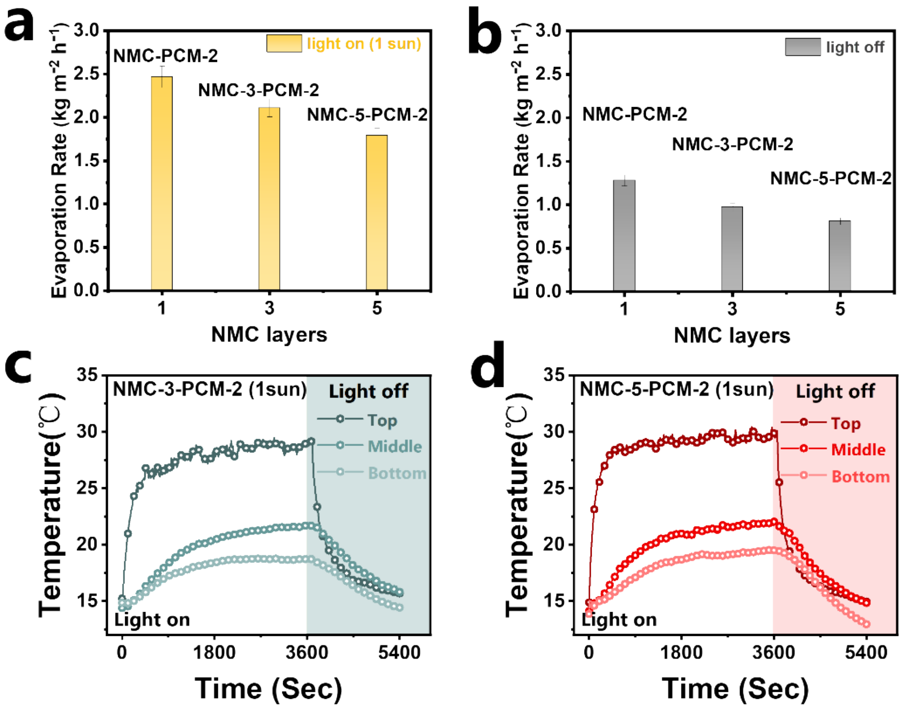

Figure S15. (a) Evaporation rate of NMC-PCM-2, NMC-3-PCM-2 and NMC-5-PCM-2 under 1 sun illumination and (b) after turning off the light source. (c) Temperature response profiles of NMC-3-PCM-2 and NMC-5-PCM-2 when the solar illumination turns on and off under 1 sun illumination, respectively.

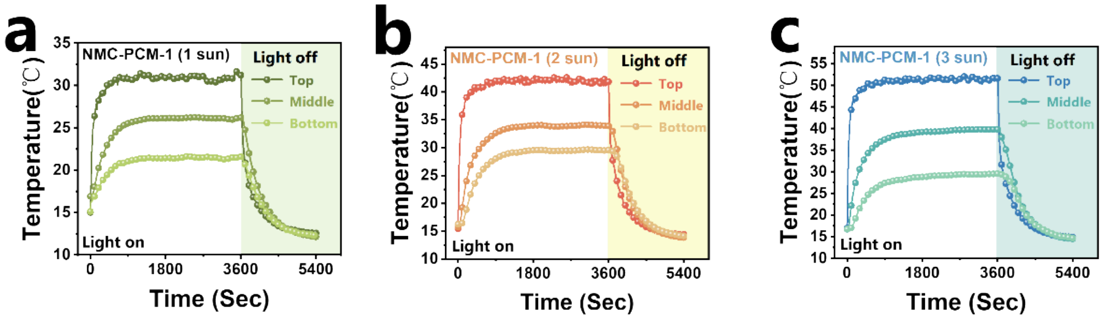

Figure S16. Temperature response profiles of NMC-PCM-1 when the solar illumination turns on and off under different irradiation of (a) 1, (b) 2, and (c) 3 sun, respectively.

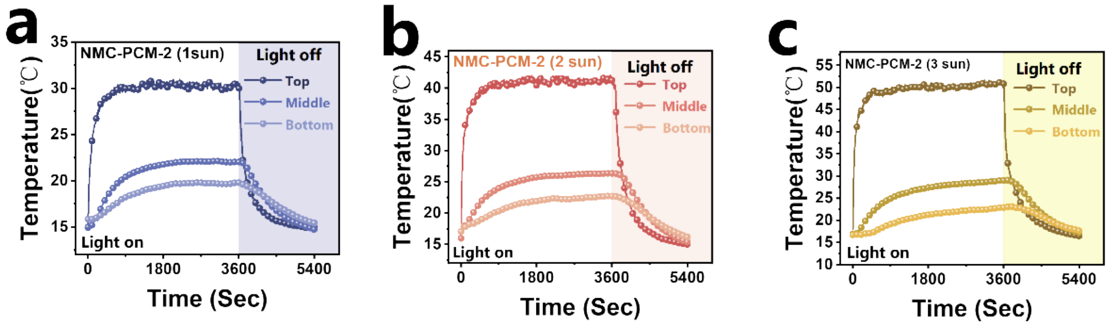

Figure S17. Temperature response profiles of NMC-PCM-2 when the solar illumination turns on and off under different irradiation of (a) 1, (b) 2, and (c) 3 sun, respectively.

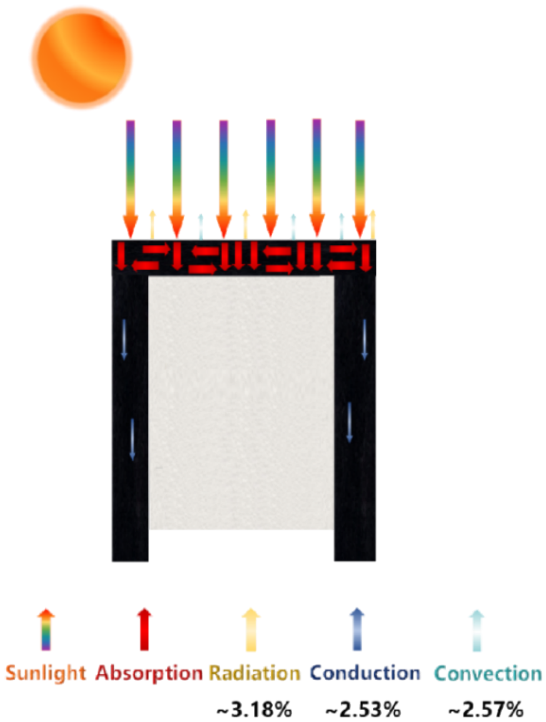

Figure S18. Energy balance and heat loss diagram of NMC-PCM-3 evaporator during the solar vapor generation process.

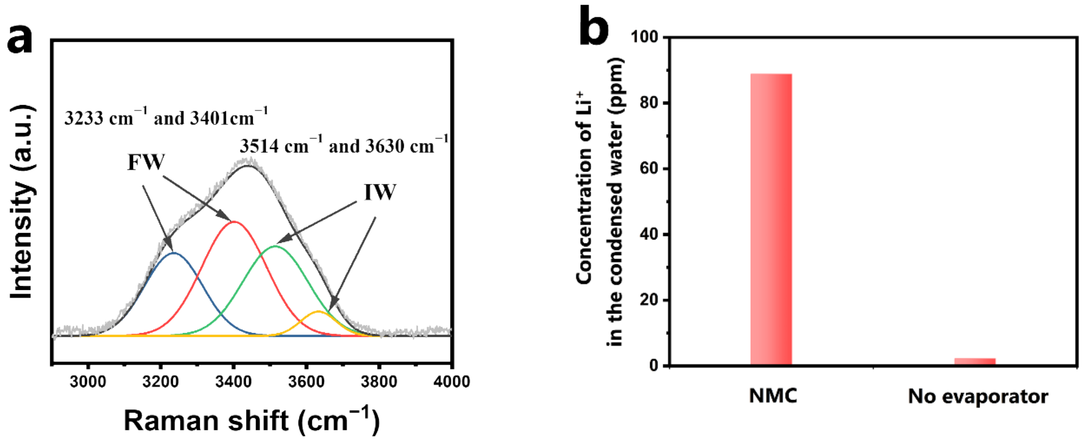

Figure S19. (a) Raman spectrum of the wet-state NMC. (b) Concentration of Li^+ in the condensed water of NCF and without evaporators under 1 Sun irradiation.

Note: To further elucidate the reduction in the water evaporation enthalpy due to the formation of water cluster in the NMC system, we performed an experiment to demonstrate the evaporation of NMC confined water in the form of water cluster. In traditional evaporation systems, water evaporates in the form of water monomer. The water cluster has been demonstrated that could be vaporized by less energy compared with monomer in bulk water.[1-3]

To prove water-cluster evaporation, we added LiCl, a non-volatile electrolyte salt into bulk water to be evaporated. This is because when evaporating as water cluster, Li^+ is taken away. As shown in Figure S13, we prepared the LiCl solution with a concentration of 500 ppm, and evaporated it through traditional evaporation from bulk water and through solar-thermal evaporation at NCF surface. The Li^+ concentration in the condensate evaporated using NMC (88.8 ppm) is greatly higher than that of the condensate evaporated by conventional evaporation (2.2 ppm).

These results above indicate that evaporation of water using NMC is most likely to evaporate as the water cluster.

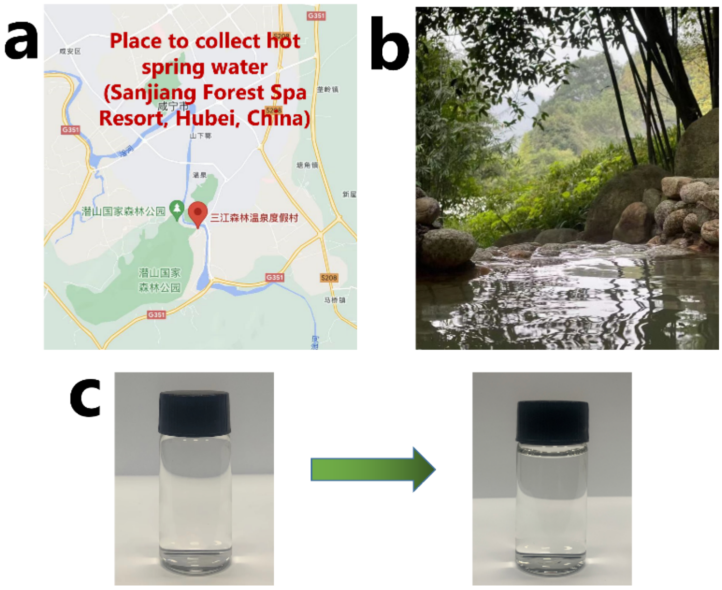

Figure S20. (a) The location and (b) photograph of the place to collect hot spring water (Xianning, Hubei, China). (c) Photographs of the hot spring water and the condensed water.

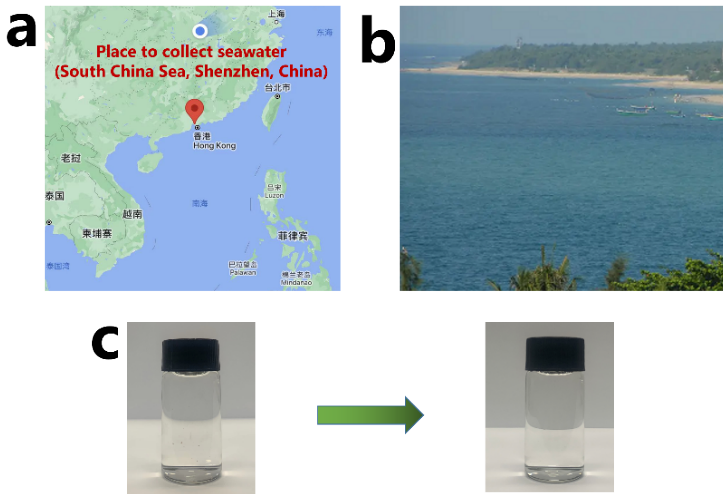

Figure S21. (a) The location and (b) photograph of the place to collect seawater (South China Sea, Shenzhen, China). (c) Photographs of the seawater and the condensed water.

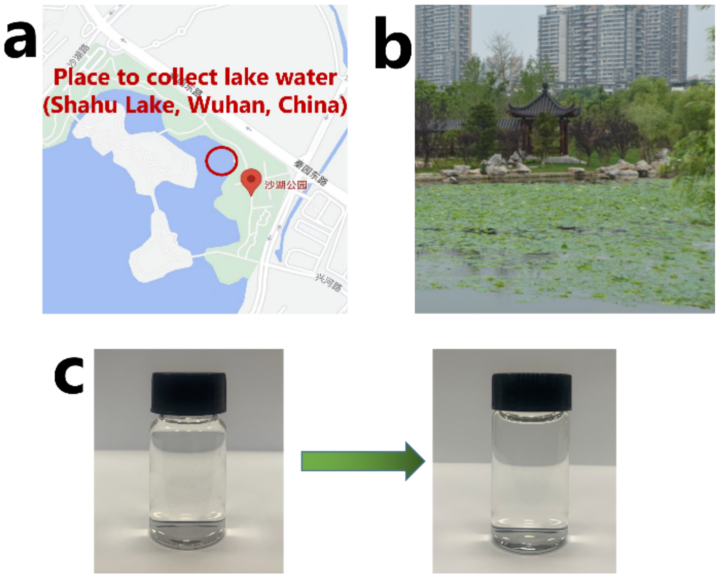

Figure S22. (a) The location and (b) photograph of the place to collect lake water (Shahu Lake, Wuhan, China). (c) Photographs of the lake water and the condensed water.

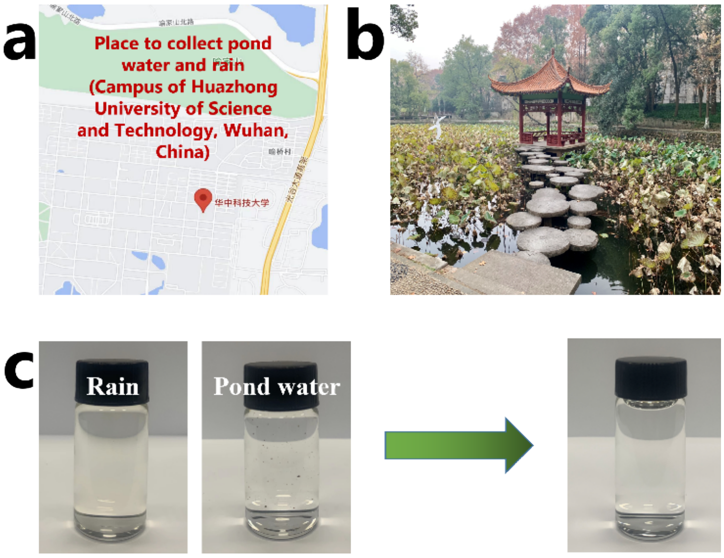

Figure S23. (a) The location and (b) photograph of the place to collect rain and pond water Campus of Huazhong University of Science and Technology, Wuhan, China). (c) Photographs of the rain/pond water and the condensed water.

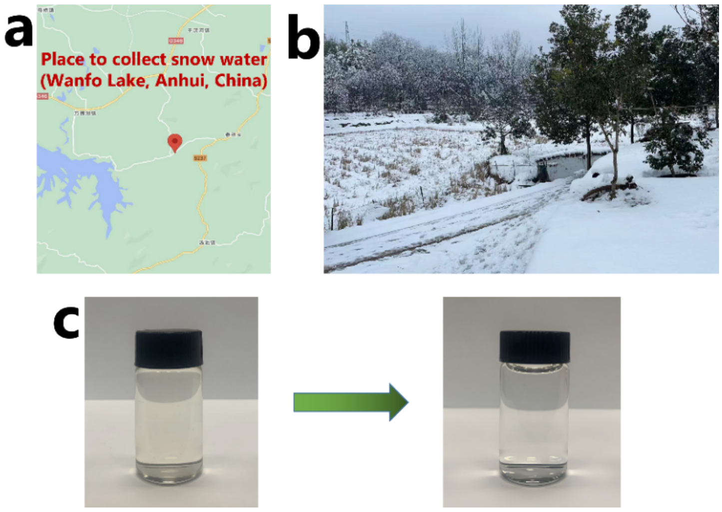

Figure S24. (a) The location and (b) photograph of the place to collect snow water (Wanfo Lake, Anhui, China). (c) Photographs of the snow water and the condensed water.

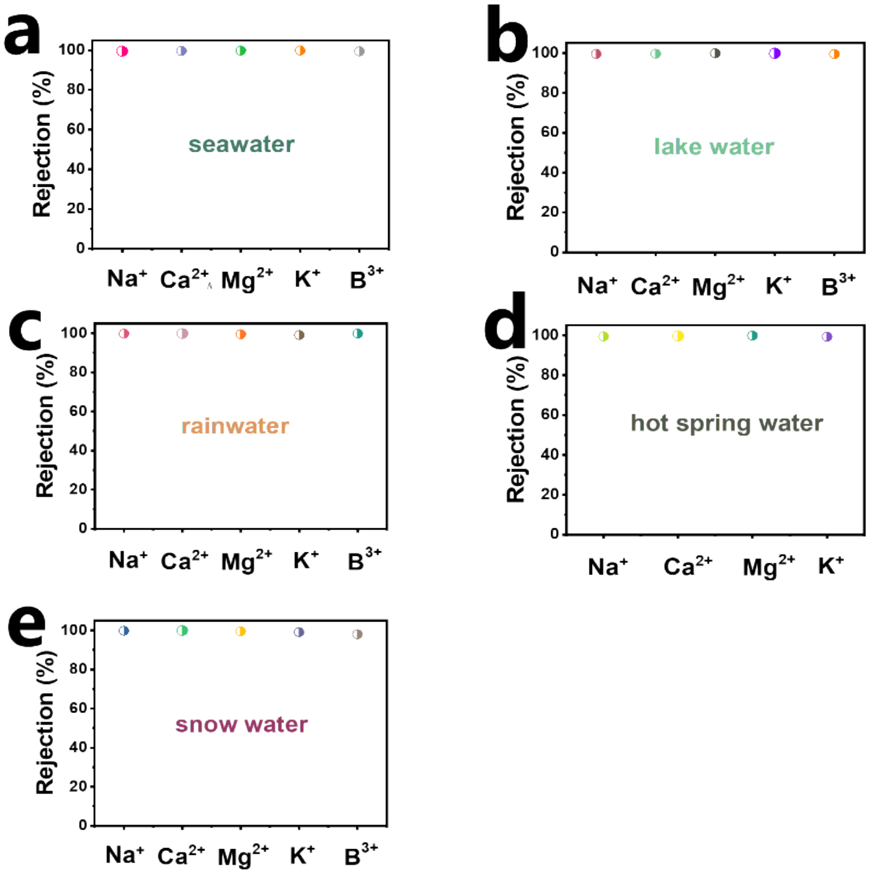

Figure S25. The ion rejection of (a) seawater, (b) lake water, (c) rainwater, (d) hot spring water, (e) snow water and (f) heavy metal ion solution undergoing the solar driven water purification under one sun illumination.

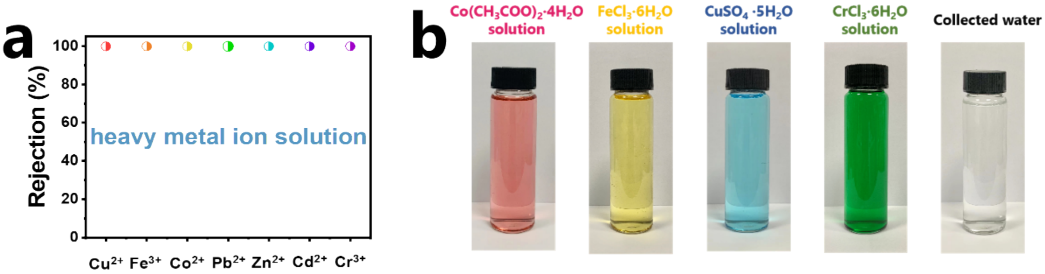

Figure S26. (a) The ion rejection of heavy metal ion solution undergoing the solar energy-driven wastewater purification under one sun illumination. (b) Digital photographs of heavy metal ion solution undergoing the solar energy-driven wastewater purification.

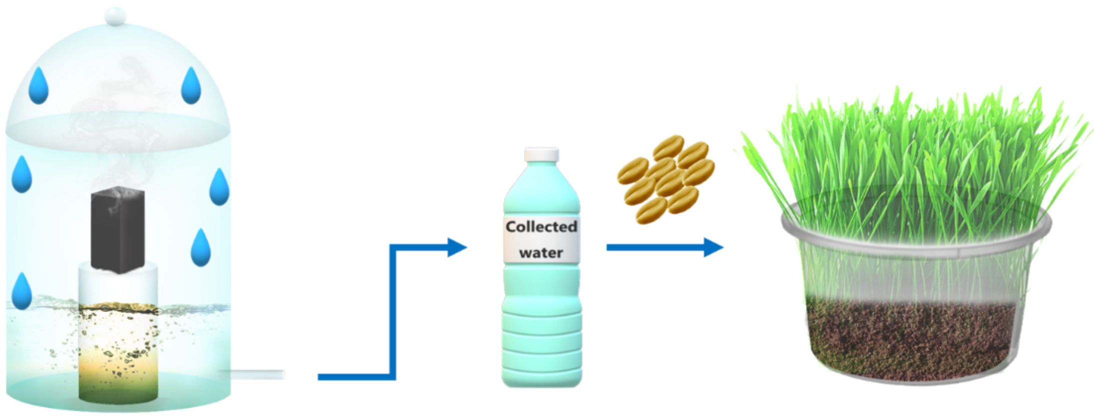

Figure S27. The experimental set-up for desalination–cultivation system.

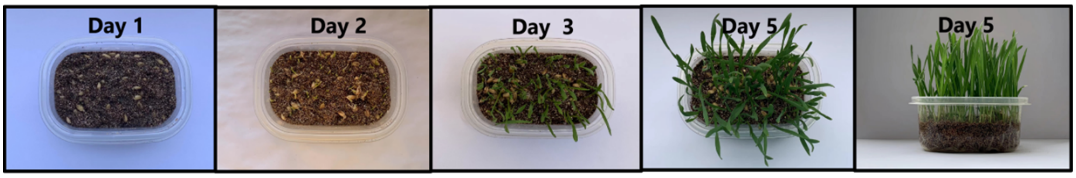

Figure S28. Digital photographs of wheat seeds grown at different times using desalinated seawater.

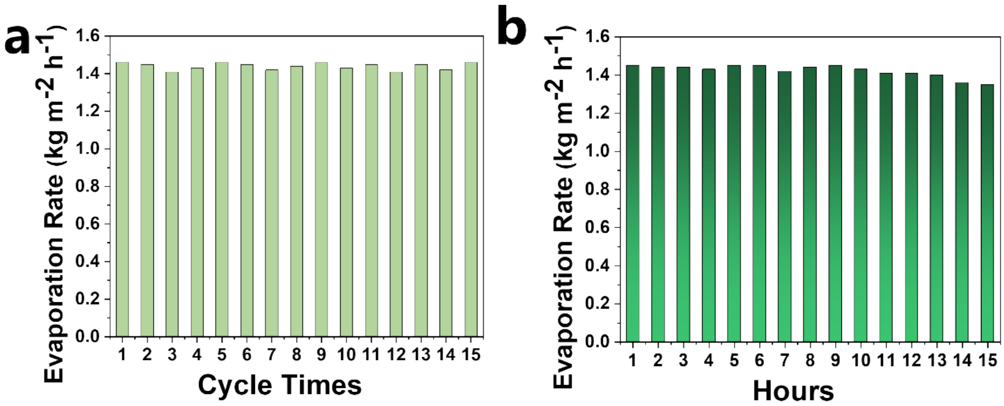

Figure S29. (a)Evaporation rate cycle performance and (b) long-term stability test of NMC-PCM-3 under one sun illumination for 1 hour and then lights off.

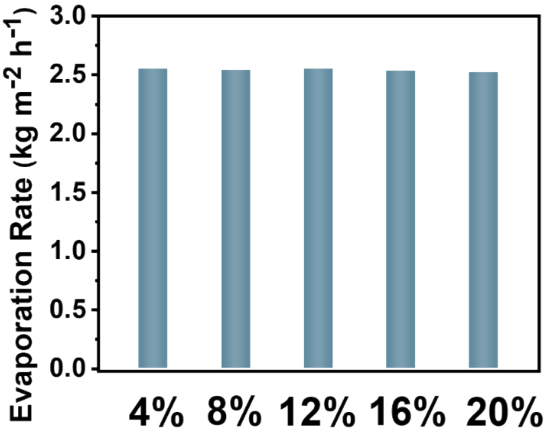

Figure S30. Evaporation rates of NMC-PCM-3 in NaCl solution with different concentrations.

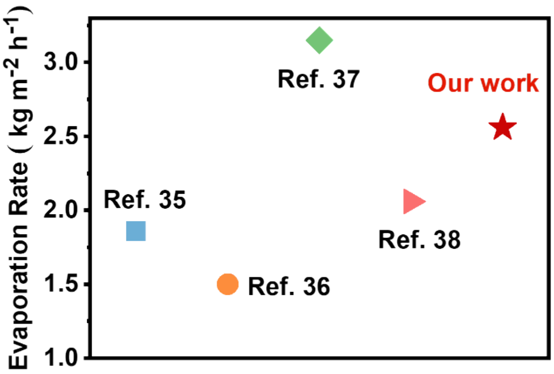

Figure S31. Evaporation rates of MOF-based photothermal materials under 1 sun illumination.

Table S1. The specific surface area of air-laid paper and NMC.

Materials	Air-laid paper	NMC
Specific surface area(m^2/g)	0.011	5.316

Table S2. The comparison of the evaporation rate using various photothermal materials under one sun illumination.

Materials		Evaporation systems	Evaporation rate (kg m^{-2} h^{-1})	Cycle number	Ref.
Semiconductor	Black TiOx nanoparticles	2D	0.80	5	1
	Black titania film	2D	1.30	10	2
	TiO_x hollow nanotubes	2D	1.17	-	3
	Black amorphous Al-Ti-O nanostructure	2D	1.03	10	4
	MoOx HNS Membrane	2D	1.26	10	5
	PTCNFAs	3D	2.89	10	6
Metallic plasmonic	Au nanoflowers silica gel	3D	1.36	-	7
	Black silver nanostructures	2D	1.32	10	8
	Cuprous telluride nanowire	2D	1.40	20	9
	Thin-film black gold membrane	2D	0.67	-	10
	Au AAO	3D	0.63	-	11
	Aufilter film	2D	1.15	-	12
Polymers	PDA/BNC membrane	3D	1.00	5	13
	Polypyrrole coated stainless steel mesh	2D	0.92	5	14
	Kapok fibers-PPy aerogels	3D	1.38	15	15
	Monolithic polymer foam	3D	1.17	100	16
	Polypyrrole Dopamine Nanofiber	3D	1.39	10	17
	Porphyrin/aniline-based conjugated microporous polymers	3D	1.31	5	18
Carbon-based	cPCO/CNT foam	3D	1.26	-	19
	CB/PMMA PAN membrane	2D	1.30	6	20
	COF/rGO	3D	3.69	7	21
	PFS@rGO	3D	1.38	20	22
	Wood/CNTs membrane	3D	0.95	10	23
	Porous carbon	3D	1.97	16	34
This work	**NMC**	**3D**	**2.55**	**15**	_

Table S3. The comparison of the evaporation rate using various MOF-based photothermal materials under one sun illumination.

Materials	Evaporation rate ($kg\ m^{-2}\ h^{-1}$)	Ref.
Cu-BTC MOFs@PANI	1.86	35
Cu-CAT-1 MHSs	1.50	36
Fe-MOF hybrid hydrogel	3.20	37
Cu-CAT-1 MOF membrane	2.07	38
This work	2.55	-

Table S4. An overall calculation of the cost of materials.

Material	Cost
Air-laid paper	0.2 \$ m^{-2}
nickel acetate	50.04 \$ Kg^{-1}
HHTP	55600 \$ Kg^{-1}
Natural wood pulp sponge	1.44 \$ L^{-1}
Organic paraffin	5.95 \$ Kg^{-1}
Aluminum foil	0.1 \$ m^{-2}
Pearl cotton	0.48 \$ m^{-2}
NMC-PCM-3	3.9 \$ each

Reference

[1] J. Tang, T. Zheng, Z. Song, Y. Shao, N. Li, K. Jia, Y. Tian, Q. Song, H. Liu and G. Xue, Realization of low latent heat of a solar evaporator via regulating the water state in wood channels. *ACS Applied Materials & Interfaces*. 2020, **12**, 18504-18511.

[2] X. Zhou, F. Zhao, Y. Guo, B. Rosenberger and G. Yu Architecting highly hydratable polymer networks to tune the water state for solar water purification. *Science advances*. 2019, **5**, eaaw5484.

[3] F. Zhao, X. Zhou, Y. Shi, X. Qian, M. Alexander, X. Zhao, S. Mendez, R.Yang, L. Qu and G. Yu, Highly efficient solar vapour generation via hierarchically nanostructured gels. *Nature nanotechnology*. 2018, **13**, 489-495.

[4] M. Ye, J. Jia, Z. Wu, C. Qian, R. Chen, P. G. O'Brien, W. Sun, Y. Dong and G. A. Ozin, Synthesis of Black TiO_xNanoparticles by Mg Reduction of TiO_2Nanocrystals and their Application for Solar Water Evaporation. *Advanced Energy Materials*. 2017, **7**, 1601811.

[5] G. Zhu, J. Xu, W. Zhao and F. Huang, Constructing Black Titania with Unique Nanocage Structure for Solar Desalination. *ACS Appl Mater Interfaces*. 2016, **8**, 31716-31721.

[6] T. Mei, J. Chen, Q. Zhao and D. Wang, Nanofibrous Aerogels with Vertically Aligned Microchannels for Efficient Solar Steam Generation. *ACS Appl Mater Interfaces.* 2020, **12**, 42686-42695.

[7] L.Yi, S. Ci, S. Luo, P. Shao, Y. Hou and Wen, Z. Scalable and low-cost synthesis of black amorphous Al-Ti-O nanostructure for high-efficient photothermal desalination. *Nano Energy*. 2017, **41**, 600-608.

[8] Q. Lu, Y. Yang, J. Feng and X. Wang, Oxygen-Defected Molybdenum Oxides Hierarchical Nanostructure Constructed by Atomic-Level Thickness Nanosheets as an Efficient Absorber for Solar Steam Generation. *Solar RRL*. 2019, **3**, 1800277.

[9] J. Wang, Y. Li, L. Deng, N. Wei, Y. Weng, S. Dong, D. Qi, J. Qiu, X. Chen and T. Wu, High-Performance Photothermal Conversion of Narrow-Bandgap Ti_2O_3 Nanoparticles. *Adv Mater*. 2017, **29**, 1603730.

[10] M. Gao, C. K. Peh, H. T. Phan, L. Zhu and G. W. Ho, Solar Absorber Gel: Localized Macro-Nano Heat Channeling for Efficient Plasmonic Au Nanoflowers Photothermic Vaporization and Triboelectric Generation. *Advanced Energy Materials*. 2018, **8**, 1800711.

[11] J. Chen, J. Feng, Z. Li, P. Xu, X. Wang, W. Yin, M. Wang, X. Ge and Y. Yin,

Space-Confined Seeded Growth of Black Silver Nanostructures for Solar Steam Generation. *Nano Lett*. 2019, **19,** 400-407.
[12] C. Chen, H. Liu, H. Wang, Y. Zhao and M. Li, A scalable broadband plasmonic cuprous telluride nanowire-based hybrid photothermal membrane for efficient solar vapor generation. *Nano Energy*. 2021, **84**, 105868.
[13] K. Bae, G. Kang; S. K. Cho, W. Park, K. Kim and W. J. Padilla, Flexible thin-film black gold membranes with ultrabroadband plasmonic nanofocusing for efficient solar vapour generation. *Nat Commun*. 2015, **6**, 10103.
[14] L. Zhou, S. Zhuang, C. He, Y. Tan, Z. Wan and, J. Zhu, Self-assembled spectrum selective plasmonic absorbers with tunable bandwidth for solar energy conversion. *Nano Energy*. 2017, **32**, 195-200.
[15] C. Liu, J. Huang, C.E. Hsiung, Y. Tian, J. Wang, Y. Han and A. Fratalocchi, High-Performance Large-Scale Solar Steam Generation with Nanolayers of Reusable Biomimetic Nanoparticles. *Advanced Sustainable Systems*. 2017, **1**, 1600013.
[16] X. Wu, S. Cao, D. Ghim, Q. Jiang, S. Singamaneni and Y. S. Jun, A thermally engineered polydopamine and bacterial nanocellulose bilayer membrane for photothermal membrane distillation with bactericidal capability. *Nano Energy*. 2021, **79**, 105353.
[17] L. Zhang, B.Tang, J. Wu, R. Li and P. Wang, Hydrophobic Light-to-Heat Conversion Membranes with Self-Healing Ability for Interfacial Solar Heating. *Adv Mater*. 2015, **27**, 4889-4894.
[18] P. Mu, W. Bai, Y. Fan, Z. Zhang, H. Sun, Z. Zhu, W. Liang and A. Li, Conductive hollow kapok fiber-PPy monolithic aerogels with excellent mechanical robustness for efficient solar steam generation. *Journal of Materials Chemistry A*. 2019, **7**, 9673-9679.
[19] Q. Chen, Z. Pei, Y. Xu, Z. Li, Y. Yang, Y. Wei and Y. Ji, A durable monolithic polymer foam for efficient solar steam generation. *Chem Sci*. 2018, **9**, 623-628.
[20] X. Ma, X. Jia, H. Gao and D. Wen, Polypyrrole-Dopamine Nanofiber Light-Trapping Coating for Efficient Solar Vapor Generation. *ACS Appl Mater Interfaces*. 2021, **13**, 57153-57162.
[21] C. Li, S. Cao, J. Lutzki, J. Yang, T. Konegger, F. Kleitz and Y. Liao, A Covalent Organic Framework/Graphene Dual-Region Hydrogel forEnhanced Solar-Driven Water Generation *J. Am. Chem. Soc.* 2022, **144**, 3083-3090.
[22] L. Zhao, L. Wang, J. Shi, X. Hou, Q. Wang, Y. Zhang, Y. Wang, N. Bai, J. Yang,

J. Zhang, B. Yu and C. Guo, Shape-Programmable Interfacial Solar Evaporator with Salt-Precipitation Monitoring Function. *ACS Nano*. 2021, **15**, 5752-5761.
[23] W. Xu, X. Hu, S. Zhuang, Y. Wang, X. Li, L. Zhou, S. Zhu and J. Zhu, Flexible and Salt Resistant Janus Absorbers by Electrospinning for Stable and Efficient Solar Desalination. *Advanced Energy Materials*. 2018, **8**, 1702884.
[24] J. Yang, Y. Pang, W. Huang, S. K. Shaw, J. Schiffbauer, M. A. Pillers, X. Mu, S. Luo, T. Zhang and Y. Huang, Functionalized graphene enables highly efficient solar thermal steam generation. *ACS nano*. 2017, **11**, 5510-5518.
[25] T. Chen, S. Wang, Z. Wu, X. Wang, J. Peng, B. Wu, J. Cui, X. Fang, Y. Xie and N. Zheng, A cake making strategy to prepare reduced graphene oxide wrapped plant fiber sponges for high-efficiency solar steam generation. *Journal of Materials Chemistry A*. 2018, **6**, 14571-14576.
[26] C. Chen, Y. Li, J. Song, Z. Yang, Y. Kuang, E. Hitz, C. Jia, A. Gong, F. Jiang, J. Y. Zhu, B. Yang, J. Xie and L. Hu, Highly Flexible and Efficient Solar Steam Generation Device. *Adv Mater*. 2017, **29**, 1701756.
[27] G. Chen, Z. Jiang, A. Li, X. Chen, Z. Ma and H. Song, Cu-based MOF-derived porous carbon with highly efficient photothermal conversion performance for solar steam evaporation. *Journal of Materials Chemistry A*. 2021, **9**, 16805-16813.
[28] Z. Li, X. Ma, D. Chen, X. Wan, X. Wang, Z. Fang and X. Peng, Polyaniline-Coated MOFs Nanorod Arrays for Efficient Evaporation-Driven Electricity Generation and Solar Steam Desalination. *Adv Sci*. 2021, **8**, 2004552.
[29] Q. Ma, P. Yin, M. Zhao, Z. Luo, Y. Huang, Q. He, Y. Yu, Z. Liu, Z. Hu, B. Chen and H. Zhang, MOF-Based Hierarchical Structures for Solar-Thermal Clean Water Production. *Adv Mater*. 2019, **31**, 1808249.
[30] Y. Guo, H. Lu, F. Zhao, X. Zhou, W. Shi and G. Yu, Biomass-Derived Hybrid Hydrogel Evaporators for Cost-Effective Solar Water Purification. *Adv Mater*. 2020, **32**, 1907061.
[31] X. Ma, Z. Li, Z. Deng, D. Chen, X. Wang, X. Wan, Z. Fang and X. Peng, Efficiently cogenerating drinkable water and electricity from seawater via flexible MOF nanorod arrays. *Journal of Materials Chemistry A*. 2021, **9**, 9048-9055.